Data Access Statement: The X-ray crystallographic coordinates for the structure reported in this study have been deposited at the Cambridge Crystallographic Data Centre (CCDC), under deposition number 2106845. These data can be obtained free of charge from the Cambridge Crystallographic Data Centre via www.ccdc.cam.ac.uk/data_request/cif. The Mathematica notebooks used for the implementation of the theoretical models of spin dynamics and electron paramagnetic resonance are available from the corresponding authors upon reasonable request.

Supplementary Information: Discriminating ferrotoroidic from antiferrotoroidic ground states using a $3d$ quantum spin sensor

Kieran Hymas,[1,*] Alessandro Soncini,[2,†] Kuduva R. Vignesh,[3] Deepanshu Chauhan,[4] Abinash Swain,[4] Sophie L. Benjamin,[5] Dipanti Borah,[4] Maheswaran Shanmugam,[4] Wolfgang Wernsdorfer,[6] Gopalan Rajaraman,[4,‡] Stuart K. Langley,[7,§] and Keith S. Murray[8,¶]

[1] *Commonwealth Scientific and Industrial Research Organisation (CSIRO), Clayton, Victoria 3168, Australia*
[2] *Department of Chemical Sciences, University of Padova, Via Marzolo 1, 35131 Padova, Italy*
[3] *Department of Chemical Sciences, Indian Institute of Science Education and Research (IISER) Mohali, Sector-81, SAS Nagar, Mohali-140306, Punjab, India*
[4] *Department of Chemistry, Indian Institute of Technology Bombay, Mumbai 400076, India*
[5] *School of Science and Technology, Nottingham Trent University, Nottingham, NG11 8NS, UK*
[6] *Institute of Quantum Materials and Technologies, Karlsruhe Institute of Technologies, 76344, Eggenstein-Leopoldshafen, Germany*
[7] *Department of Natural Sciences, Chemistry, Manchester Metropolitan University, Manchester, M15 6BH, UK*
[8] *School of Chemistry, Monash University, Clayton, 3800, Australia*

(Dated: October 30, 2024)

CONTENTS

* kieran.hymas@csiro.au
† alessandro.soncini@unipd.it
‡ rajaraman@chem.iitb.ac.in
§ s.langley@mmu.ac.uk
¶ keith.murray@monash.edu

I. CRYSTAL DATA AND STRUCTURE REFINEMENT FOR $CrDy_3$

Supplementary Table 1: Crystal data and structure refinement. [a] Including solvate molecules. [b] Graphite monochromator. [c] $R_1 = \sum ||F_O| - |F_C|| / \sum |F_O|$, $wR_2 = \left(\sum \left[w(F_O^2 - F_C^2)^2\right] / \sum \left[w(F_O^2)^2\right]\right)^{1/2}$.

	1
Formula[a]	$Dy_3CrC_{36}H_{50}O_{27}$
M/ [g mol^{-1}]	1609.03
Crystal system	Orthorhombic
Space group	*Pnma*
a/[Å]	19.4471(4)
b/[Å]	21.1752(4)
c/[Å]	17.3815(6)
α/[°]	90
β/[°]	90
γ/[°]	90
V/[Å^{-1}]	7157.6(2)
T/K	123(2)
Z	4
ρ_{calc} [g cm^{-3}]	1.471
Λ^{b} /[Å]	0.71073
Data Measured	34446
Ind. Reflns	8982
R_{int}	0.0414
Reflns with $I > 2\sigma(I)$	7003
Parameters	391
Restraints	35
R_1^{c} (obs), wR_2^{c} (all)	0.0645, 0.1729
Goodness of fit	1.119
Largest residuals/[e Å^{-3}]	4.711, −1.523

II. RESULTS FROM *AB INITIO* COMPLETE ACTIVE SPACE CALCULATIONS FOR $CrDy_3$

Supplementary Table 2: RASSI energies (cm^{-1}) of the 8 lowest-lying Kramer's doublets (KDs) for isolated Dy^{III} ions in compound **1**.

KDs	Dy1	Dy2	Dy3
1	0.0	0.0	0.0
2	152.6	140.1	129.2
3	225.8	216.4	202.8
4	264.8	246.2	224.3
5	320.4	281.3	247.1
6	345.7	306.2	286.5
7	386.5	352.3	338.7
8	431.5	427.5	425.1

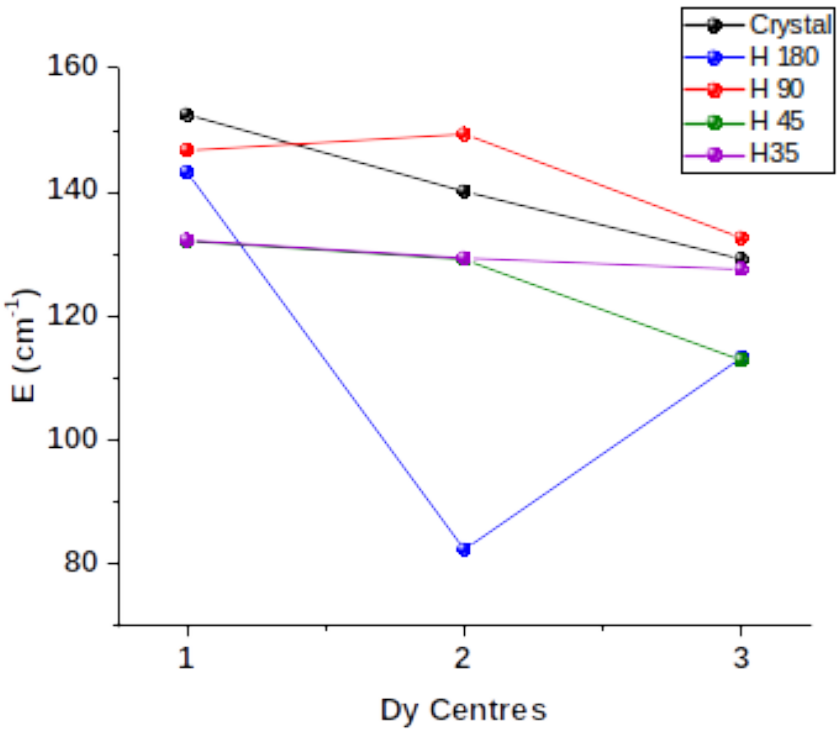

Supplementary Figure 1: CASSCF computed ground to first excited state energy gaps in Dy^{III} ions of $CrDy_3$ as function of H_2O orientation. Black data points depict results of calculations conducted on the $CrDy_3$ crystal structure. The blue and red data points are results from the same calculations however with the H-O bonds of each water molecule oriented parallel and perpendicular (respectively) to the plane of the isonicotinate ligand which coordinates with the relevant Dy^{III} and Cr^{III} ions.

Supplementary Table 3: Table of g tensors for the 8 lowest lying Kramer's doublets (KDs) of the Dy^{III} ions in compound **1**.

KDs	g	Dy1	Dy2	Dy3
1	g_x	0.012	0.014	0.045
	g_y	0.025	0.021	0.059
	g_z	19.560	19.470	19.379
2	g_x	0.698	0.603	1.199
	g_y	1.090	0.691	1.549
	g_z	15.524	15.668	15.143
3	g_x	3.784	2.820	1.050
	g_y	4.629	4.095	2.791
	g_z	11.558	11.542	10.761
4	g_x	0.376	9.646	1.119
	g_y	4.851	6.030	5.435
	g_z	9.393	0.999	13.347
5	g_x	0.359	2.118	1.91
	g_y	5.187	4.439	5.824
	g_z	10.148	13.528	13.104
6	g_x	1.430	0.114	0.287
	g_y	4.351	0.572	0879
	g_z	15.508	17.156	18.014
7	g_x	0.143	0.309	0.286
	g_y	0.615	0.586	0.483
	g_z	18.874	18.546	18.764
8	g_x	0.119	0.080	0.030
	g_y	0.291	0.095	0.058
	g_z	19.288	19.478	19.586

Supplementary Table 4: RASSI energies (cm^{-1}) of the 8 lowest-lying Kramer's doublets (KDs) for isolated Dy^{III} ions in compound **1** with water molecules rotated parallel to isonicotinate ligands.

KDs	Dy1	Dy2	Dy3
1	0.0	0.0	0.0
2	143.2	82.3	113.3
3	218.7	121.9	155.0
4	256.9	180.514	209.1
5	310.1	213.9	256.3
6	358.8	247.3	291.7
7	377.0	159.8	376.0
8	392.4	369.7	412.0

Supplementary Table 5: RASSI energies (cm^{-1}) of the 8 lowest-lying Kramer's doublets (KDs) for isolated Dy^{III} ions in compound **1** with water molecules rotated perpendicular to isonicotinate ligands.

KDs	Dy1	Dy2	Dy3
1	0.0	0.0	0.0
2	146.7	149.4	132.6
3	240.7	262.1	221.6
4	285.1	327.1	274.7
5	328.3	364.9	302.3
6	393.8	396.9	343.2
7	420.6	484.3	364.2
8	492.0	534.7	500.7

Supplementary Table 6: RASSI energies (cm^{-1}) of the 8 lowest-lying Kramer's doublets (KDs) for isolated Dy^{III} ions in compound **1** with water molecules rotated 45° to isonicotinate ligands.

KDs	Dy1	Dy2	Dy3
1	0.0	0.0	0.0
2	132.1	129.1	112.9
3	191.1	162.9	167.0
4	230.4	231.2	192.6
5	276.0	295.7	221.0
6	330.9	330.6	262.8
7	379.8	345.6	345.7
8	444.4	389.4	365.8

Supplementary Table 7: RASSI energies (cm^{-1}) of the 8 lowest-lying Kramer's doublets (KDs) for isolated Dy^{III} ions in compound **1** with water molecules rotated 135° to isonicotinate ligands.

KDs	Dy1	Dy2	Dy3
1	0.0	0.0	0.0
2	132.3	129.4	127.5
3	207.4	173.2	198.2
4	239.5	218.5	235.5
5	285.7	273.5	253.3
6	339.3	326.7	313.8
7	376.3	343.7	355.7
8	436.8	362.2	432.6

III. RELEVANT $CrDy_3$ POPULATIONS FOR SINGLE-CRYSTAL MAGNETISATION

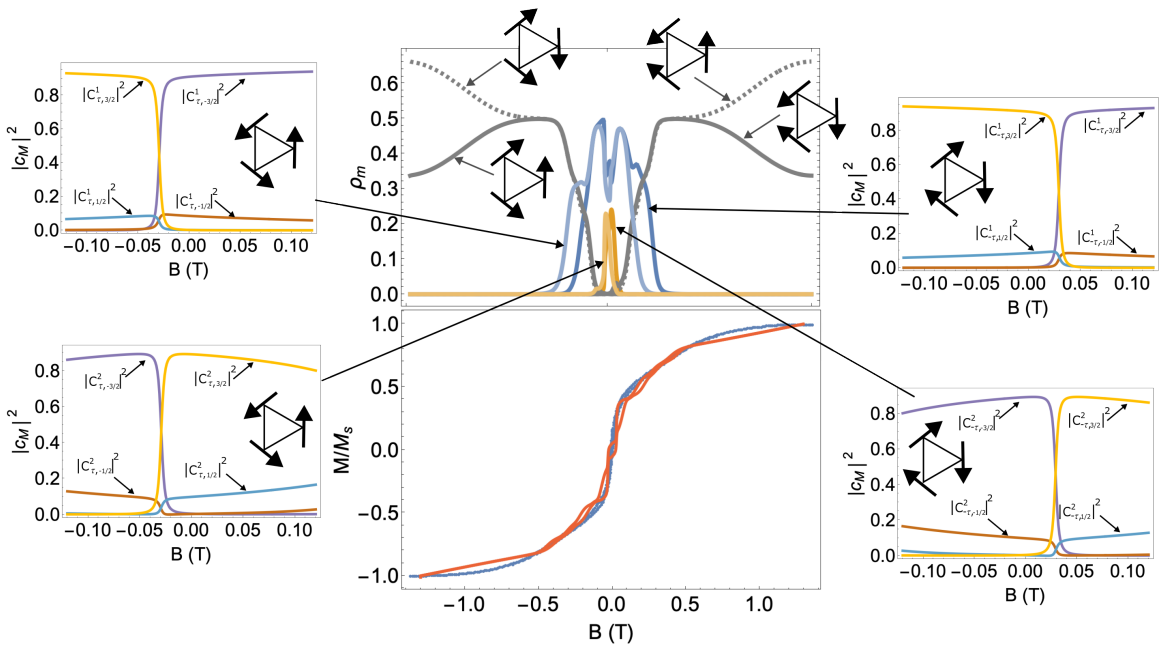

Supplementary Figure 2: (top) Time evolution of the $CrDy_3$ spin state populations on forward trace of the applied magnetic field at a rate of $\omega = 0.28$ T s^{-1}. The colour coding of the populations matches that of the Zeeman diagram in the main text with the blue and yellow curves depicting the time evolution of the first and second excited Cr^{III} spin states, respectively, with a clockwise (dark) and anticlockwise (light) Dy_3 toroidal configuration. The grey solid lines depict the time-evolution of the Dy_3 magnetic configuration populations. The time-evolution of the four adiabatically evolving Cr^{3+} spin states (with toroidal Dy_3 configurations) are also shown to illustrate the quantum superposition of the Cr^{III} spin states owing to competing magnetic interactions. (bottom) Magnetic hysteresis simulation against experiment from the main text for reference.

IV. SUPPLEMENTARY NOTE 1: ALTERNATIVE EXPLANATION FOR THE $CrDy_3$ SICKLE-SHAPED MAGNETISATION

In this section, we propose an alternative explanation for the sickle-shaped single-crystal magnetisation for $CrDy_3$ which entails a magnetic response originating solely from the Cr^{3+} ion, weakly coupled to the toroidal ground state of the Dy_3 triangular lanthanide moiety. Using the same theoretical model from the main text, with the anisotropy axes of all paramagnetic species fixed by the *ab initio* results, we simulated the experimental single-crystal magnetisation curve (Figure 2 of the main text) by allowing the exchange coupling parameters J_1 and J_2, and the magnetic field orientation η_F and ϕ_F to vary.

Given the small hysteresis loops of magnetization observed in the experimental curves, we assume that the tracing field evolves *quasi*-statically with respect to the fast fluctuating Cr^{III}. Hence, at each field value the sum of the molecular Hamiltonian H_{mol}, and Zeeman Hamiltonian H_{Zee}, can be diagonalised for each semi-classical Dy^{III} spin configuration $\mathbf{m}$ of $CrDy_3$, to yield the 32 instantaneous eigenstates $|\mathbf{m},\varphi_i\rangle = \sum_{M_{\mathrm{Cr}}} C^i_{\mathbf{m},M_{\mathrm{Cr}}} |\mathbf{m}\rangle \otimes |M_{\mathrm{Cr}}\rangle$ $(i = 1,\ldots,4)$ with energies $E_{|\mathbf{m},\varphi_i\rangle}$. As in the main text, the field dependence of the energies $E_{|\mathbf{m},\varphi_i\rangle}$ and amplitudes $C^i_{\mathbf{m},M_{\mathrm{Cr}}}$ is implied and we choose a quantisation axis for Cr^{III} along the axis of the applied field. Thus, with our effective model, we simulate the single-crystal magnetisation of $CrDy_3$ and find excellent agreement with the experimental data using the values $J_1 = 0.2$ cm^{-1}, $J_2 = -0.6$ cm^{-1}, $\eta_F = 40°$ and $\phi_F = 50°$ (see Figure **??**a).

The Zeeman spectrum of $CrDy_3$ plotted in Figure **??**b reveals that no level crossings occur between the toroidal ground state configurations and single or double-flipped Dy^{III} magnetic states (shown in grey) indicating that the

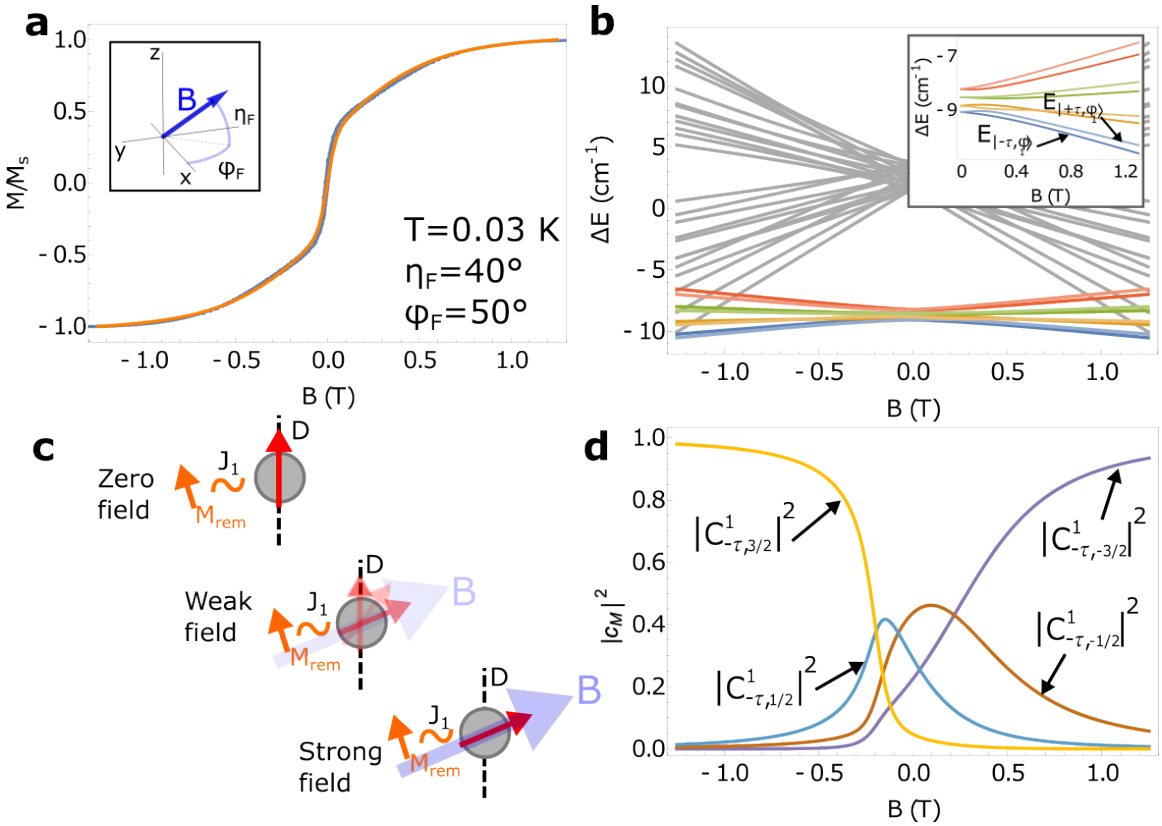

Supplementary Figure 3: Theoretical simulation and interpretation of single-crystal μ-SQUID experiments. **a** Normalised simulated single-crystal magnetisation curve (orange) against μ-SQUID single-crystal measurements (blue) at $T = 0.03$ K and with a field oriented $\eta_F = 40°$ out-of-plane with azimuthal angle $\phi_F = 50°$. **b** Zeeman spectrum of the 32 dimensional Hilbert space of the effective $CrDy_3$ model. The toroidal manifolds are shown in colour whereas the single spin-flipped dysprosium magnetic states have been greyed out for clarity. The inset shows a close-up of the Zeeman spectrum of the 8 dimensional toroidal manifold for positive fields. **c** Schematic representation of the applied magnetic field (purple arrow) torquing the Cr^{III} quantum spin sensor after aligning to the remnant magnetic moment (orange arrow) of the Dy_3 triangle, M_{rem}, along its principal magnetic easy axis (dashed line). **d** Squared amplitudes of the $|-\tau,\phi_1\rangle$ Cr^{III} wavefunction against applied field.

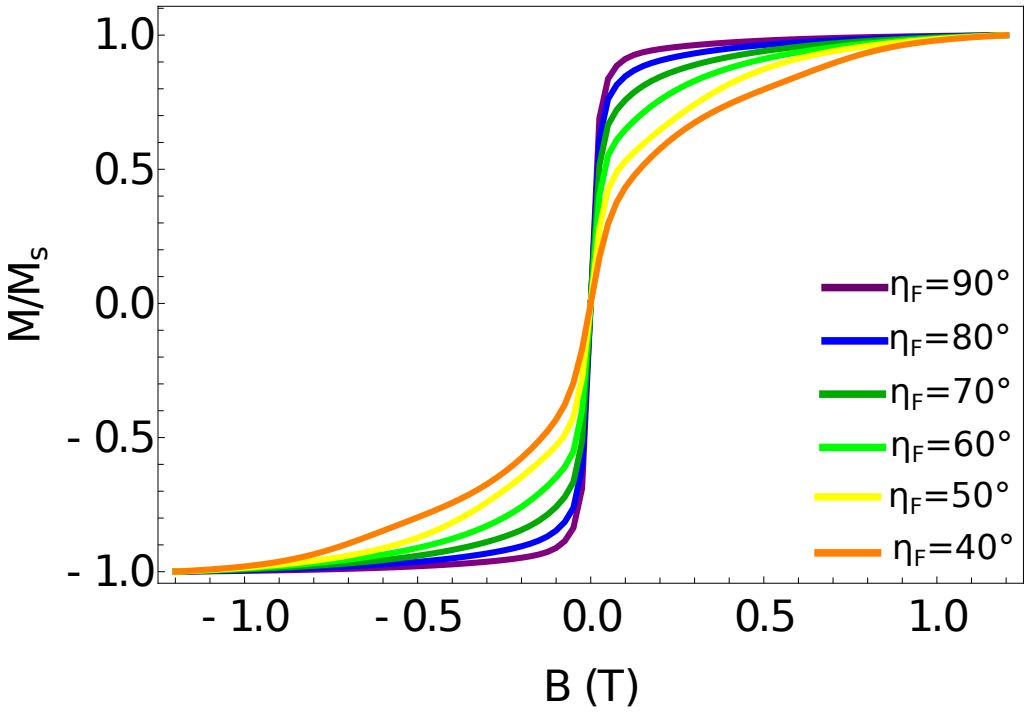

Supplementary Figure 4: Simulated single-crystal magnetisation for $CrDy_3$ at $T = 0.03$ K using the effective theoretical model presented above. Keeping all parameters from the main text fixed, we vary the out-of-plane angle η_F of the magnetic field.

single-crystal magnetisation is dominated by the magnetic response of the Cr^{III} ion. Nevertheless, the experimental and simulated single-crystal magnetisation differs markedly from a typical Brillouin curve expected for an isolated, free-fluctuating Cr^{III} spin.

A schematic illustration of the magnetic response of the Cr^{III} quantum spin to the external field is shown in Figure **??**c. In the absence of a magnetic field, the Cr^{III} spin aligns along it's easy axis, roughly perpendicular to the triangular plane. By virtue of the ferromagnetic exchange coupling J_1, the spin is preferentially aligned with the remnant magnetic moment of the Dy_3 triangle, M_{rem}, which is almost collinear with the Cr^{III} principal anisotropy axis. The application of a small positive field exerts a magnetic torque on the Cr^{III} spin leading to a quantum superposition of $|M_{\mathrm{Cr}}\rangle$ spin states and hence to a slow rise in the squared amplitude of the ground state $|M_{\mathrm{Cr}}\rangle = -3/2$ projection along the axis of the field (see purple curve in Figure **??**d). Without any source of magnetic anisotropy, i.e. for a free-fluctuating spin, this alignment would be instantaneous and result in a typical Brillouin magnetisation curve. The sickle-shaped magnetisation in $CrDy_3$ at positive fields, is reflected in the square of $C^1_{-\tau,-3/2}$ and for negative fields in the square of the time-reversed $C^1_{\tau,3/2}$ amplitudes. Naturally, the detection of toroidal states in the single-crystal magnetisation of $CrDy_3$ depends upon dominant thermal population of the ground state (blue curve in Figure **??**b) of the ground toroidal manifold. Since the splitting of these states is roughly 0.5 cm^{-1}, toroidal moment sensing here is possible up to ~ 1 K.

In Figure **??** we show the angle dependence of this signal as a result of varying the canting of the external magnetic field η_F. When the field is aligned approximately along the anisotropy axis of Cr^{3+} and the remnant magnetic moment of the Dy_3 triangle, an approximate Brouillon function is recovered. Deviating from this preferential axis however, introduces a competition between the applied field and the intrinsic magnetic anisotropy axes of the molecule, for the alignment of the Cr^{3+} magnetic moment resulting in the sickle-shaped magnetisation response. In Figure **??** we deconstruct the effects of zero-field splitting of the ground Cr^{III} quartet and magnetic coupling to the remnant magnetisation in Dy_3 on the single-crystal magnetisation of $CrDy_3$. When both interactions are absent, a Brillouin curve typical of a free-fluctuating spin $\frac{3}{2}$ is recovered (Figure **??**a) which is far from the experimentally observed sickle-shaped magnetisation. It is evident from panels b and c, that neither the inclusion of zero-field splitting nor magnetic coupling to M_{rem} alone recovers the experimental curve but rather a combination of the two (Figure **??**d).

Despite the striking agreement between our model and the experimental single-crystal magnetisation results, we exclude this explanation for the sickle-shaped single-crystal magnetisation on the basis that the large value of J_2, the Dy-Dy intramolecular exchange coupling, required to isolate the Cr^{3+} spin dynamics from Dy^{3+}, introduces a

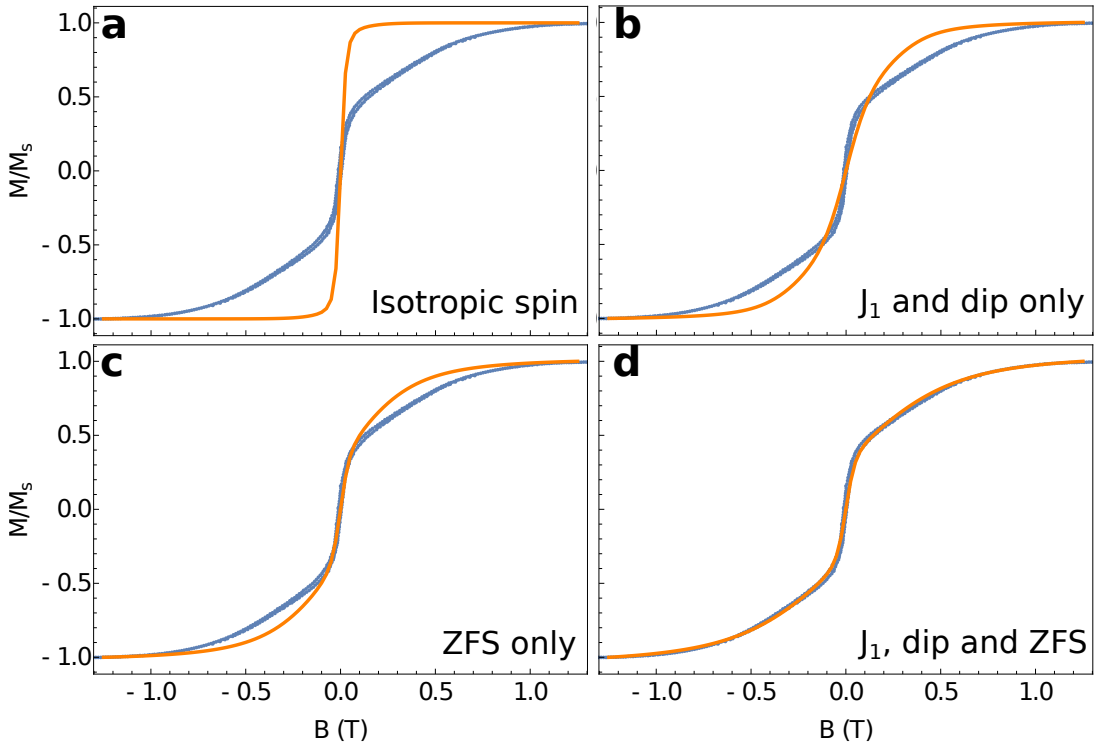

Supplementary Figure 5: Decomposition of interactions leading to $CrDy_3$ magnetic response. Single-crystal magnetisation computed with our model (orange curves) superimposed to experimental data (blue curves) using parameters specified in the main text however now with **a** no zero-field splitting of Cr^{III} and no coupling to M_{rem}, **b** coupling to M_{rem} only, **c** *ab initio* determined zero-field splitting only and **d** all interactions included.

characteristic sigmoidal shape to the isothermal powder magnetisation (See Figure **??**) which we do not observe in experiment. This mechanism is worth mentioning, nevertheless, as a potential alternative explanation for sickle-shaped magnetisation curves in other mixed $3d$-$4f$ SMT systems with large intramolecular lanthanide exchange.

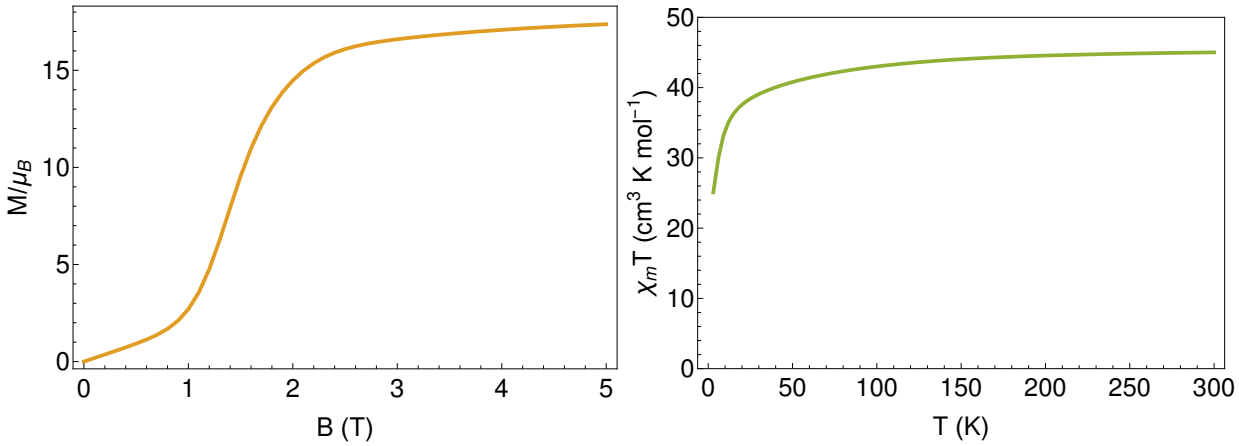

Supplementary Figure 6: (left) Simulated powder magnetisation for $CrDy_3$ at $T = 2$ K using parameters described above. To simulate the random orientation of molecules in the powder we integrate the magnetisation over a Lebedev sphere with 146 points. (right) Simulated magnetic susceptibility versus temperature for $CrDy_3$ using parameters from above. Here we utilise the theoretical model in the main text however, to arrive at the correct high temperature limit associated with thermal population of all Kramers doublets of the Dy^{III} ions, we add in the *ab initio* computed susceptibilities and subtract away the contribution $(\chi T)_0$ from the ground Kramers doublets of Dy^{III} and the ground quartet of Cr^{III} to avoid double counting, i.e. $\chi T = (\chi T)_{\text{model}} + (\chi T)_{\text{ab initio}} - (\chi T)_0$.

V. ANGLE-DEPENDENT μ-SQUID SIMULATIONS FOR SENSING FERROTOROIDIC OR ANTIFERROTOROIDIC GROUND STATES IN $CuDy_6$

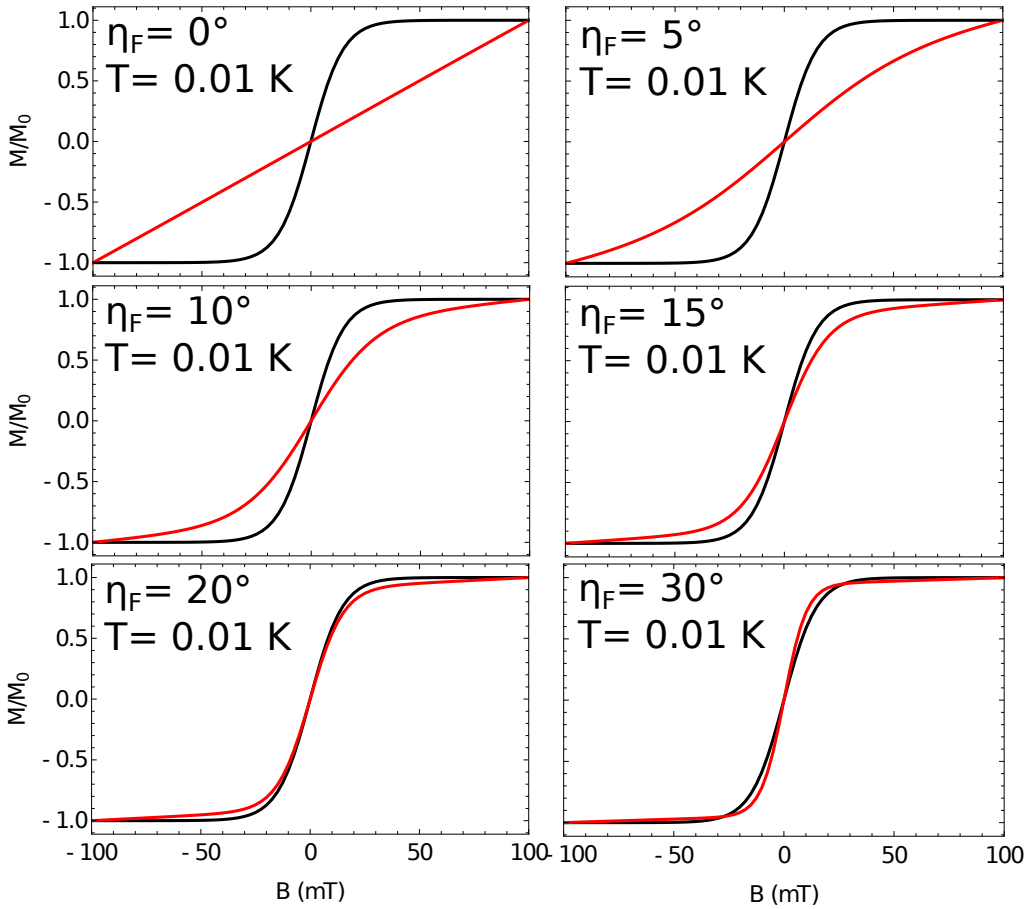

Supplementary Figure 7: Simulated single-crystal magnetisation for $CuDy_6$ with a ferrotoroidic (black) and antiferrotoroidic (red) ground state at $T = 0.01$ K using the effective theoretical model presented in the main text. Keeping all parameters from the main text fixed and restricting the field sweeping domain to -100 mT $\leq B \leq 100$ mT, we vary the out-of-plane angle η_F of the magnetic field for each figure. Note that for a ferrotoroidic ground state (black curve), the single-crystal magnetisation is unchanging with η_F, a response typical of an isotropic spin $S = \frac{1}{2}$. When the antiferrotoroidic Dy_3-Dy_3 configuration is the ground state, the single crystal magnetisation (red curve) is sensitive to the field orientation η_F.

VI. FURTHER INFORMATION ON ELECTRON PARAMAGNETIC RESONANCE SIMULATIONS FOR $CuDy_6$

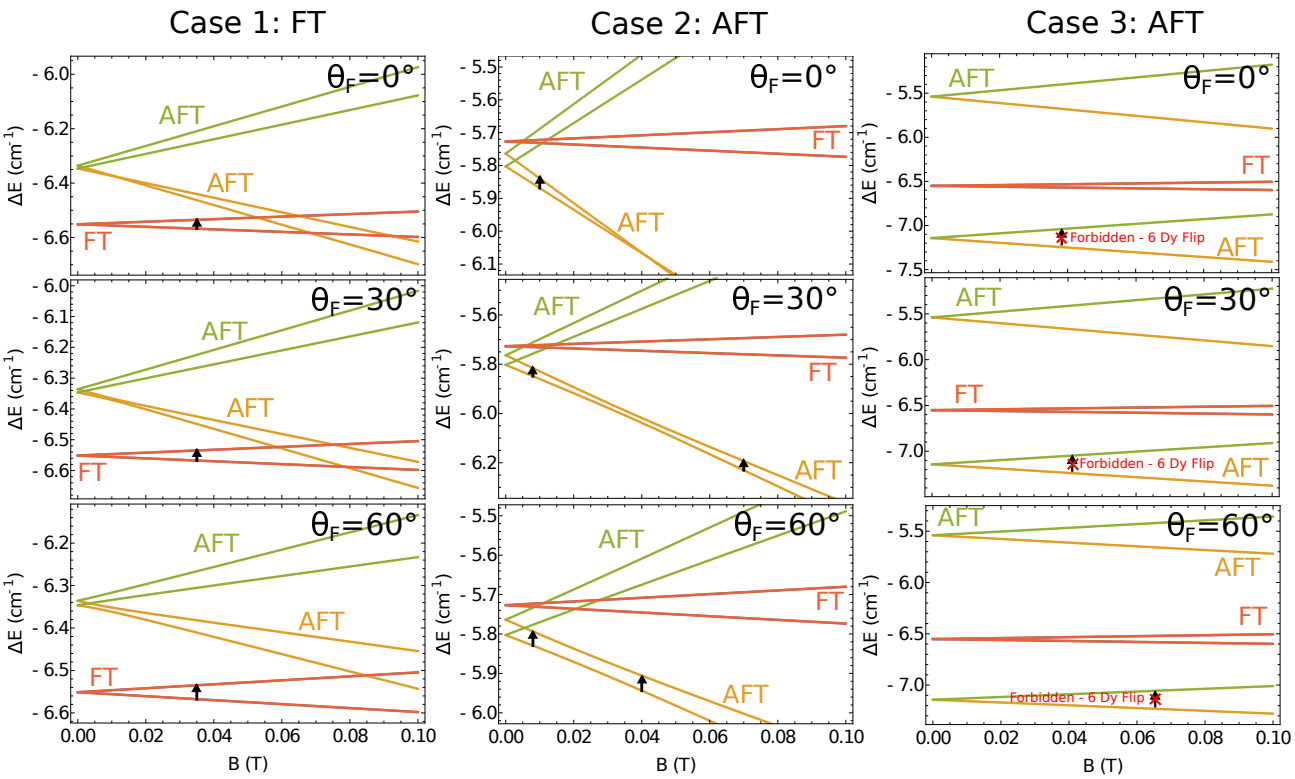

Supplementary Figure 8: Zeeman diagrams for three cases of $CuDy_6$ ground state with field oriented in θ_F from the molecular z axis (i.e. the direction of out-of-plane canting of Dy magnetic axes). Black arrows indicate possible transitions proportional to $\nu = 6$ GHz radiation. Case 1 is achieved with $J_1 = -0.08$ cm^{-1}, $J_2 = -0.043$ cm^{-1}, $\eta = 6.63°$ and $\phi = 0.63°$. Case 2 is achieved with $J_1 = -0.08$ cm^{-1}, $J_2 = -0.043$ cm^{-1}, $\eta = 15°$ and $\phi = 0.63°$. Case 3 is achieved with $J_1 = -1$ cm^{-1}, $J_2 = -0.043$ cm^{-1}, $\eta = 6.63°$ and $\phi = 0.63°$. For case 1, a resonant gap between the Cu spin states with ferrotoroidic Dy configurations (red) occurs at $B \sim 35$ mT and does not change with field orientation. In case 2, resonant gaps occur around $B \sim 25 - 50$ mT as well as $B \sim 70$ mT between Cu spin states and one of the antiferrotoroidic Dy configurations (yellow); the position of these resonances is highly sensitive to field orientation leading to broadening of the EPR spectrum. In case 3, no signal is observed since the only resonant transitions are between states from different antiferromagnetic manifolds i.e. would require 6 simultaneous Dy magnetic moment flips.

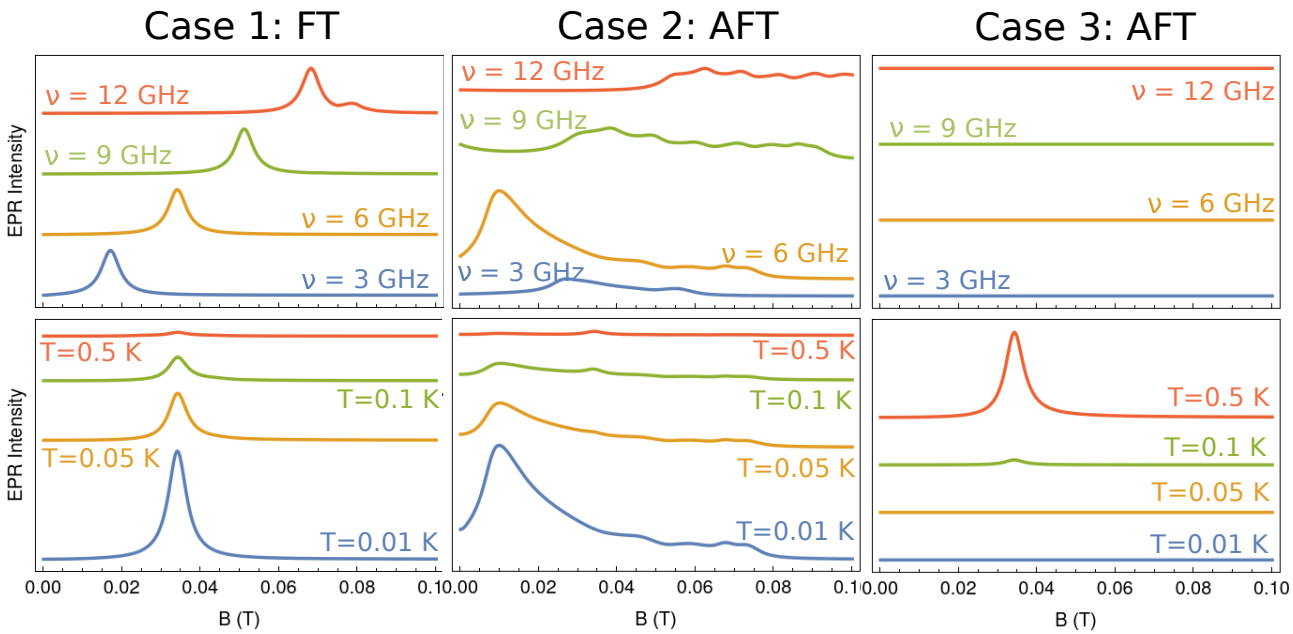

Supplementary Figure 9: Simulated powder EPR spectra for three cases of $CuDy_6$ ground state. The top row illustrate the zero temperature frequency dependence of the spectra in each of the three different cases and the bottom row shows the temperature dependence (for $\nu = 6$ GHz) of each ground state case. Spectra are offset for clarity. Both frequency and temperature dependence of case 1 is typical of an isotropic $S = 1/2$ spin. A series of convoluted peaks occur in case 2 as a result of the anisotropy induced by coupling of the Cu spin to the remnant magnetisation of the ground antiferrotoroidic configuration, as temperature is increased the signal flattens out. For case three, a characteristic blank spectra is observed apart from the emergence of hot transitions between $T = 0.1 - 0.5$ K resulting from spin transitions in the excited ferrotoroidic manifold.